

# Landau-Zener interference at bichromatic driving

Florian Forster,<sup>1</sup> Max Mühlbacher,<sup>1</sup> Ralf Blattmann,<sup>2</sup> Dieter Schuh,<sup>3</sup>  
Werner Wegscheider,<sup>4</sup> Stefan Ludwig,<sup>1,5</sup> and Sigmund Kohler<sup>6</sup>

<sup>1</sup>Center for NanoScience & Fakultät für Physik, LMU-Munich, 80539 München, Germany

<sup>2</sup>Department of Physics and Astronomy, Aarhus University, Ny Munkegade 120, 8000 Aarhus C, Denmark

<sup>3</sup>Fakultät für Physik, Universität Regensburg, 93040 Regensburg, Germany

<sup>4</sup>Solid State Physics Laboratory, ETH Zurich, 8093 Zurich, Switzerland

<sup>5</sup>Paul-Drude-Institut für Festkörperelektronik, Hausvogteiplatz 5–7, 10117 Berlin, Germany

<sup>6</sup>Instituto de Ciencia de Materiales de Madrid, CSIC, 28049 Madrid, Spain

(Dated: June 14, 2021)

We investigate experimentally and theoretically the interference at avoided crossings which are repeatedly traversed as a consequence of an applied ac field. Our model system is a charge qubit in a serial double quantum dot connected to two leads. Our focus lies on effects caused by simultaneous driving with two different frequencies. We work out how the commensurability of the driving frequencies affects the symmetry of the interference patterns both in real space and in Fourier space. For commensurable frequencies, the symmetry depends sensitively on the relative phase between the two modes, whereas for incommensurable frequencies the symmetry of monochromatic driving is always recovered.

PACS numbers: 73.63.-b, 03.67.-a, 03.65.Yz, 73.63.Kv,

## I. INTRODUCTION

Landau-Zener-Stückelberg-Majorana (LZSM) interference protocols have been explored experimentally in various solid-state implementations ranging from Josephson junctions [1–8] to quantum dot based devices [9–11]. Besides demonstrating quantum coherence, LZSM interference allows one to explore dissipative effects in a predominantly coherent dynamics and determine system parameters such as the coherence time  $T_2$  or the inhomogeneous decay time  $T_2^*$  [4, 10, 11]. Previous studies considered monochromatic driving, in one case with an additional sudden parameter switching at a low rate [8], which may be an insignificant restriction if one merely aims at studying the coherence and decoherence of solid-state qubits. Driving with two or more frequencies of the same order and different phases, however, opens up a multitude of additional possibilities which are worthwhile exploring.

Building on two recent projects, one studying LZSM interference in a double quantum dot (DQD) charge qubit [11] and one applying bichromatic driving to a single dot realizing a Lissajous rocking ratchet [12], here we combine bichromatic driving with LZSM interference in the DQD shown in Fig. 1(a) and explore the cases of commensurable versus incommensurable frequencies. Depending on the phase between its two components, bichromatic driving with commensurable frequencies may break time reversal symmetry, which is particularly visible in the Fourier transformed of the LZSM interference pattern [13]. For the quasi-periodic driving with two incommensurable frequencies, by contrast, we find irrespective of the phase difference the symmetry properties of the monochromatic case.

The theoretical approaches exploring driven dissipative systems often rely on the time-periodicity of the external field. Such methods applied in the context of LZSM

interference include the mapping to a time-independent problem via a rotating-wave approximation [13–16], the computation of stationary phases [4, 17], and the decomposition of a quantum master equation into the Floquet states of the central system [16, 18]. For transport problems, LZSM patterns have been calculated ignoring interactions with Floquet scattering theory [19, 20]. Taking into account two-particle interactions or a quantum

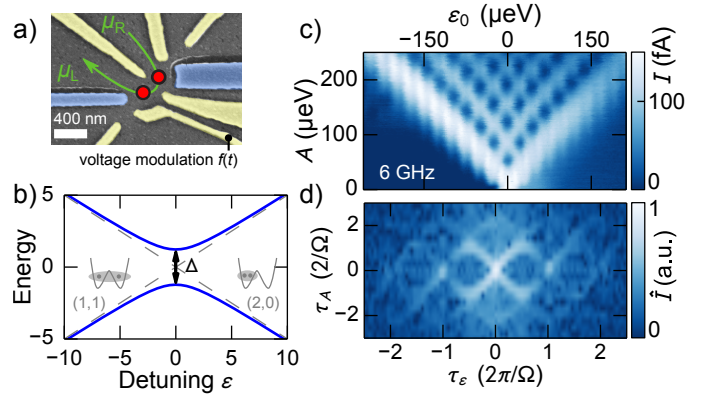


FIG. 1. (a) Scanning electron micrograph of the wafer surface. The GaAs surface is dark gray, gold gates are shown in yellow and cobalt gates in blue. Red filled circles sketch the approximate quantum dot positions in the two-dimensional electron system 85 nm beneath the surface. The voltage on the lower right gate is radio frequency modulated with the function  $f(t)$ . (b) Avoided crossing of the eigen states (solid lines) composed of the singlets (dashed lines) with charge configuration (1, 1) and (2, 0) (visualized in double well sketches), which mix via the interdot tunnel coupling  $\Delta$ . (c) Measured LZSM pattern  $I(\epsilon_0, A)$  for monochromatic driving with frequency 6 GHz. (d) Corresponding Fourier transformed LZSM pattern (plotted with a logarithmic color scale).

heat bath, transport experiments can be described with a more realistic Floquet master equation approach [11]. While a Floquet ansatz can be generalized to bichromatic driving straightforwardly [21, 22], the resulting scheme may be numerically demanding and only a few explicit results can be found in the literature [22]. Here we develop a more efficient method including the case of driving with two incommensurable frequencies. It combines two known methods, namely a Floquet matrix representation [23] and the solution of a recurrence equation by matrix continued fractions [24].

This article is arranged as follows: In Sec. II, we present our experimental setup. In Sec. III, we introduce our theoretical description and derive a Floquet method for the solution of master equations with two incommensurable drivings. Section IV is devoted to the analytical and numerical computation of LZSM interference pattern, their symmetries, and the comparison to the experimental results. Additional measured data can be found in Appendix A. Moreover, in Appendix B we sketch the two Floquet methods for single-frequency driving that we combine to obtain our numerical scheme.

## II. EXPERIMENT

In our experiments, we measured LZSM interference patterns at the avoided crossing of two charge states in the DQD presented in Fig. 1(a). The states are the singlets formed by  $(2,0)$  and  $(1,1)$ , where  $(n_1, n_2)$  denotes the number of electrons in the left ( $n_1$ ) and right ( $n_2$ ) dot. The avoided crossing, sketched in Fig. 1(b) as a function of the detuning energy  $\epsilon$  between the two singlets, is formed by the interdot tunnel coupling  $\Delta$ . By modulating the voltage on one of the quantum dot defining gates we modulate the detuning with a periodic function  $\epsilon = \epsilon_0 + Af(t)$  and thereby repeatedly drive the system through the avoided crossing resulting in LZSM interference. To detect the electron charge state, we apply a constant voltage  $V = (\mu_R - \mu_L)/e = 1$  mV across the DQD, where  $\mu_{L,R}$  are the chemical potentials of the leads and measure the steady state current resulting from the combination of  $V$  and the rf-modulation. We tuned our DQD such that the current is virtually exclusively caused by tunneling of single electrons via the configuration cycle  $(1,0) \rightarrow (1,1) \leftrightarrow (2,0) \rightarrow (1,0)$ . The current  $I$  is then proportional to the occupation of  $(2,0)$  and the current maxima and minima in Fig. 1(c) are a signature of the interference of the  $(2,0)$  and  $(1,1)$  singlet states as we periodically drive our DQD through their avoided crossing. Note that the transition  $(1,1) \rightarrow (2,0)$  is initially slowed down by Pauli-spin blockade [25], i.e. as long as a  $(1,1)$  triplet is occupied no current flows. Primarily due to the inhomogeneous field of on-chip nanomagnets [marked blue in Fig. 1(a)] [26] the triplet eventually decays into the  $(1,1)$  singlet and sets off the interference dynamics observed here. The interference pattern as a function of  $\epsilon_0$  and  $A$  in Fig. 1(c) is a typical example for monochro-

matic driving of the form  $f(t) = \sin(\Omega t)$  which is well understood and has been observed in various physical systems [1–7, 9–11]. The interference pattern and even more its two-dimensional Fourier transform presented in Fig. 1(d) [4, 5, 11] exhibit a high degree of symmetry.

This article is devoted to bichromatic driving of the form  $f(t) = \sin \Omega t + \eta \sin(\Omega' t + \phi)$ , where our main focus lies in two very different cases, namely commensurate versus incommensurate frequencies  $\Omega$  and  $\Omega'$ . The first corresponds to a rational  $\Omega'/\Omega$  and, thus, periodic driving, while the latter corresponds to an irrational  $\Omega'/\Omega$  and quasi-periodic driving. We will find that the two cases have quite different symmetry properties. Experimentally, one of the main challenges beyond monochromatic driving is to control the relative phases of different frequency components, a consequence of the dispersion of the transmission lines at radio-frequencies. We will, however, present a straightforward method to calibrate relative phase differences by means of symmetry considerations. Before we present our experimental results, let us sharpen our expectations by introducing a general theory for bichromatic driving.

## III. THEORETICAL DESCRIPTION

In our experiment, the electron transport from source to drain occurs via the DQD configuration cycle  $(1,1) \rightarrow (2,0) \leftrightarrow (1,0) \rightarrow (1,1)$ . Owing to the possible spin configurations, it consists of 7 states. This makes the Floquet decomposition of the density operator a demanding task for bichromatic driving, where coherences described by off-diagonal density matrix elements play a decisive role. However, the coherent interdot tunneling relevant for the LZSM interference studied here is restricted to the singlet subspace [11] in which the left dot is always occupied and a single electron charge tunnels between the two dots. For our purposes a simplifying description based on a single spinless electron tunneling between the two dots is sufficient. It is described by the Hamiltonian

$$H = \frac{\epsilon_0 + Af(t)}{2}(c_1^\dagger c_1 - c_2^\dagger c_2) + \frac{\Delta}{2}(c_1^\dagger c_2 + c_2^\dagger c_1) + Un_1 n_2, \quad (1)$$

the interdot tunneling  $\Delta$ , and the electron creation operators  $c_{1,2}^\dagger$ . The detuning  $\epsilon(t) = \epsilon_0 + Af(t)$  consists of a static component  $\epsilon_0$  and a time-dependent contribution with amplitude  $A$ . Its shape is given by a bounded periodic or quasi-periodic function  $f(t)$  with zero mean. The term with the dot occupation numbers  $n_i = c_i^\dagger c_i$  expresses the Coulomb blockade, where we assume that the Coulomb repulsion  $U$  is so strong that charge states different from those mentioned above are inaccessible.

### A. Master equation

The DQD is coupled to a source and a drain which we describe as a canonical ensemble of free electrons with chemical potentials that depend on the applied voltage. A tunnel coupling between the leads and the respective dot completes the model. With a standard second-order approach for the coupling, we eliminate the leads and obtain a Bloch-Redfield master equation for the reduced DQD density operator  $\rho$ . Its incoherent terms typically depend on the details of the system and the leads such as the temperature, the chemical potentials  $\mu_{L,R}$  of the left and right lead, the overlap between the DQD eigenstates and the localized states, as well as the DQD eigenenergies.

If all DQD chemical potentials (which here are the energies of the single-particle states) are larger than  $\mu_L$  and smaller than  $\mu_R$ , the incoherent tunnel terms assume the convenient Lindblad form such that the master equation becomes

$$\dot{\rho} = L\rho \equiv -\frac{i}{\hbar}[H(t), \rho] + \Gamma_L D(c_1)\rho + \Gamma_R D(c_2^\dagger)\rho, \quad (2)$$

with the Lindblad superoperator

$$D(x)\rho = \frac{1}{2}(2x\rho x^\dagger - x^\dagger x\rho - \rho x^\dagger x) \quad (3)$$

and the dot-lead rates  $\Gamma_{L,R}$ . The first term in Eq. (3) describes incoherent transitions induced by the operators  $c_1$  and  $c_2^\dagger$ , i.e., tunneling between the DQD and the leads. This implies that the current superoperators are given by  $J_L\rho = \Gamma_L c_1 \rho c_1^\dagger$  and  $J_R\rho = \Gamma_R c_2^\dagger \rho c_2$ , respectively. Owing to charge conservation, both yield the same time-averaged expectation value.

In quantum dots such as ours, the electrons are subjected to environmental fluctuations which affect the coherence of the DQD electrons. The environment can be described as a bath of harmonic oscillators that couple to an appropriate DQD degree of freedom. For weak coupling one may eliminate the bath to obtain a Bloch-Redfield master equation. Its coefficients are temperature dependent, which allows one to determine the effective DQD-environment coupling strength by analyzing the fading of LZSM patterns with increasing temperature [11]. However, since such computation of the dissipative kernel is rather time consuming and beyond the present scope, we take a simpler route: Within a standard approximation scheme [27], one can bring dissipation kernels to the Lindblad form

$$L_{\text{diss}} = \frac{\gamma}{2} D(x), \quad (4)$$

where  $x$  is the operator that induces dissipative transitions. In our system the relevant noise stems from charge fluctuations that couple to the DQD dipole moment. Therefore, the coupling operator is proportional to the population imbalance  $x = (n_1 - n_2)/2$  [28], while the effective rate  $\gamma$  collects all prefactors. For relatively low

temperatures,  $\gamma$  depends on the detuning and the tunnel coupling and can be estimated as  $\gamma = \pi\alpha\Delta^2/(\epsilon_0^2 + \Delta^2)^{1/2}$  [29]. The dimensionless dissipation strength in a similar system has been determined as  $\alpha = 1.5 \times 10^{-4}$  [11]. We replace the decoherence rate by its average in the relevant range and use the value  $\gamma = 1 \text{ neV}/\hbar$ .

The coupling to the dissipative environment via the operator  $n_1 - n_2$  is of the ‘‘longitudinal’’ type investigated in Ref. [13]. Purely ‘‘longitudinal’’ coupling results in triangular structures in  $I(\epsilon_0, A)$  and anti-symmetric line shapes in  $I(\epsilon_0)$ , in contrast to Lorentzians found in our data, e.g. for horizontal slices in Fig. 1(c). However, the Lorentzians are restored already by small additional decoherence such as a ‘‘transverse’’ coupling [13] or dot-lead tunneling [11]. In our case the latter governs the shape of the peaks so that a possible tiny ‘‘transverse’’ coupling can be neglected.

### B. Two-mode Floquet transport theory

From a formal perspective, we are interested in the solution of a master equation of the form  $\dot{P} = L(t)P$ , where  $P$  may be a reduced density operator or a distribution function. For single-frequency driving of the form  $L_1 \sin(\Omega t)$ , one can make use of the time-periodicity of the long-time solution and employ the ansatz  $P(t) = \sum_k e^{ik\Omega t} p_k$  with the trace condition  $\text{tr} p_k = \delta_{k,0}$ . The resulting equation for the  $p_k$  can be solved in various ways. In particular, one may write it as a so-called Floquet matrix and numerically compute its kernel. Alternatively one may exploit the tridiagonal block structure of the equations and solve them with matrix-continued fractions. For a short summary of each method, see Appendix B. Here we extend the first method to the case of bichromatic driving with commensurable frequencies for which the Liouvillian is still periodic. For the quasi-periodic with incommensurate frequencies, we combine both methods and thereby obtain an efficient numerical scheme.

#### 1. Single-frequency driving and commensurable frequencies

Let us start the discussion for the limiting case of periodic and monochromatic driving with just one frequency  $\Omega$ . Since in the Liouvillian in Eq. (2), the time dependence is fully contained in the DQD Hamiltonian, one possibility to make use of the Floquet theorem would be to compute the Floquet states of the Hamiltonian (1) and to use them as a basis [11, 20]. This procedure is general and would allow us to consider a driving that shifts the DQD levels repeatedly across the chemical potentials of the leads, but it is numerically expensive. Since our experiment is operated with a large bias, so that such effects can be excluded we can take a more efficient route and employ the ideas of a Floquet approach directly to the master equation (2) [22]. The corresponding decom-

position solution of the master equation is straightforward and is summarized in Appendix B 1. It yields a tridiagonal block matrix whose kernel corresponds to the steady-state solution of the master equation.

If one adds a  $n$ th harmonic to the system, i.e., a contribution with the time-dependence  $\sin(n\Omega t + \varphi_n)$ , the system remains  $2\pi/\Omega$  periodic and one can still proceed as sketched above. Essentially, the Floquet matrix acquires a contribution in the  $n$ th diagonal of the block matrix, while the computation of the time-averaged steady state remains the same.

## 2. Incommensurable frequencies

We consider a master equation  $\dot{P} = L(t)P$  with bichromatic driving for which the Liouvillian is of the form

$$L(t) = L_0 + L_1 \cos(\Omega t) + L'_1 \cos(\Omega' t), \quad (5)$$

with non-rational  $\Omega'/\Omega$ . As we will argue below, for incommensurable frequencies the time-averaged steady-state solution does not depend on the relative phase between the two components of the driving. Thus, for convenience and in contrast to the rest of this work, we choose here particular phases such that the driving is given by cosine functions. Moreover,  $L(t)$  is quasi-periodic rather than periodic and the usual Floquet ansatz with a periodic long-time solution is not justified. To circumvent this problem, we employ an idea on which a propagation scheme known as  $t$ - $t'$  formalism [21, 30] is built. We replace in the last term of  $L(t)$  the time variable by  $t'$  which we will treat as an independent angle variable, i.e., we assume that all functions of  $t'$  are  $2\pi/\Omega'$  periodic. In doing so we obtain the generalized Liouvillian

$$L(t, t') = L_0 + L_1 \cos(\Omega t) + L'_1 \cos(\Omega' t') \quad (6)$$

and postulate the generalized master equation

$$\left( \frac{\partial}{\partial t} + \frac{\partial}{\partial t'} \right) Q(t, t') = L(t, t') Q(t, t'). \quad (7)$$

From the chain rule of differentiation follows directly that if  $Q(t, t')$  is a solution of the generalized master equation, then  $P(t) = Q(t, t')|_{t'=t}$  solves the original master equation. By rewriting Eq. (7) as

$$\frac{\partial}{\partial t} Q(t) = \mathcal{L}(t) Q(t), \quad (8)$$

$$\mathcal{L}(t) = L_0 + L'_1 \cos(\Omega' t') - \frac{\partial}{\partial t'} + L_1 \cos(\Omega t), \quad (9)$$

we suppress the new coordinate  $t'$  in the master equation. In this way we have obtained a time-periodic master equation with a periodic Liouvillian  $\mathcal{L}(t) = \mathcal{L}(t + 2\pi/\Omega)$  for the price of an additional degree of freedom, namely  $t'$ . Accordingly the generalized density operator  $Q$  can be decomposed as

$$Q(t) = \sum_k e^{-ik\Omega t} Q_k = \sum_{k,n} e^{-ik\Omega t} e^{-in\Omega' t'} q_{n,k}, \quad (10)$$

which corresponds to the ansatz proposed in Ref. [22]. In a formal consideration,  $Q$  is an element of the Sambe space  $\mathcal{P}(\mathcal{H}) \otimes \mathcal{T}'$  which here is composed of the projective Hilbert space  $\mathcal{P}(\mathcal{H})$  for the density operator and the space  $\mathcal{T}'$  of  $2\pi/\Omega'$  periodic functions.

The above transformation has a useful consequence, namely that  $\mathcal{L}$  defines a time-periodic problem for which the common Floquet tools known from the literature apply. In particular, we can employ the matrix-continued fraction method summarized in the Appendix B 2. For the generalized Liouvillian  $\mathcal{L}$ , the matrices  $A_n$  and  $B$  defined in the Appendix B 2 become

$$\mathcal{A}_k = L_0 \otimes \mathbb{1} + \frac{1}{2} L'_1 \otimes X + i\Omega' \mathbb{1} \otimes Z + ik\Omega \mathbb{1} \otimes \mathbb{1}, \quad (11)$$

$$\mathcal{B} = \frac{1}{2} L_1 \otimes \mathbb{1}, \quad (12)$$

where  $\mathbb{1}$  denotes the unit matrices in the space indicated by the operator order. The matrices  $X$  and  $Z$  are defined by their elements  $X_{kk'} = \delta_{k+1,k'} + \delta_{k-1,k'}$  and  $Z_{kk'} = k\delta_{kk'}$ . The last term in Eq. (11) corresponds to the decomposition of  $-\partial/\partial t$ . With  $\mathcal{A}_k$  and  $\mathcal{B}$ , the recursion in Eqs. (B7), (B8), and (B9) provides  $q_{n,0}$  and, finally, the time averaged distribution  $\overline{P(t)} = \overline{Q(t, t)} = q_{0,0}$ .

Let us argue why  $q_{0,0}$  does not depend on possible phases or time offsets in  $L(t)$ . A phase in the first time-dependent term of the Liouvillian (5) affects the recurrence relation on which the matrix-continued fractions are based. As such, it is not relevant for the iteration scheme, as shown rigorously in Appendix B 2. A phase  $\varphi'$  in the driving  $L'_1 \cos(\Omega' t)$  enters via  $\mathcal{A}_k$  such that its second term becomes  $L'_1 (e^{i\varphi'} \delta_{k+1,k'} + e^{-i\varphi'} \delta_{k-1,k'})/2$ . It can be removed by the transformation  $q_{n,k} \rightarrow q_{n,k} e^{-ik\varphi'}$ , which does not change  $q_{0,0}$ .

One might be tempted to employ the ansatz (10) also for commensurable frequencies. Then, however, the time-dependent exponential functions on the r.h.s. of Eq. (10) lose their linear independence. As a consequence, the Floquet representation is no longer unique and relations based on the orthogonality of the Floquet solutions will not hold. This is also manifest in the time-average of  $e^{-in\Omega t - ik\Omega' t}$  which would be finite not only for  $n = k = 0$ , but also for other combinations of  $n$  and  $k$ .

## IV. INTERFERENCE PATTERNS

Electron transport across the DQD requires interdot tunneling which is most pronounced when the DQD levels are in resonance with each other (and the electron tends to be delocalized between the two dots). At the resonance the adiabatic eigenstates form an avoided crossing. Our system reaches this resonance at times for which  $\epsilon_0 + Af(t) = 0$  and traverses the resonance repeatedly for sufficiently large  $A$  such that

$$A \min[f(t)] < -\epsilon_0 < A \max[f(t)]. \quad (13)$$

At the crossings, the transitions follow the scenario considered by Landau, Zener, Stückelberg, and Majorana [31–34] in which the electron wave function is split into a superposition. Repeated sweeps through the crossing lead to interference which may be constructive or destructive depending on the phase accumulated in between. Consequently the current  $I(\epsilon_0, A)$  exhibits an interference pattern in the triangle determined by Eq. (13). Analyzing this interference pattern and its Fourier transform can provide the complete information about the coherence properties of the DQD [11].

A measured example of the interference pattern and its Fourier transform for monochromatic driving  $f(t)$  is presented in Figs. 1(c),(d). The Fourier transform exhibits a characteristic arc structure with reflection symmetry at both the  $\tau_\epsilon$ -axis and the  $\tau_A$ -axis and, consequently, with point symmetry at the origin. For the case of periodic bichromatic driving, i.e. with commensurable frequencies, the mirror symmetry is generally broken and the details of the symmetry properties depend on the phase difference between the two frequency components of  $f(t)$ , see e.g. Fig. 4. For quasi-periodic bichromatic driving with incommensurable frequencies, by contrast, it turns out that the interference pattern and its Fourier transform regain the full reflection symmetries of the monochromatic case, see Fig. 5. Theoretically, the case of periodic driving can be treated correctly with the method presented in Ref. [13], while the quasi-periodic case (of incommensurable frequencies) reveals peculiarities which require the more general approach developed above.

#### A. Fourier transformed interference pattern: analytical approach to the arc structure

In the absence of interaction, Floquet scattering theory [20, 35] can be employed to find an analytic expression for the dc current  $I(\epsilon_0, A)$  through a driven DQD [19] which exhibits the main features of the characteristic interference pattern apparent in Fig. 1(c). Further, dissipation has been approximately taken into account in several analytic expressions of the interference pattern [4, 13, 16]. Computing the Fourier transform of these expressions provides the arc structure. A solution for monochromatic driving has been obtained in a stationary-phase calculation [4] and a more general solution for arbitrary periodic driving has been derived recently using the Floquet ansatz [13]. These analytic solutions are all based on the approximation  $\Delta \ll \Gamma$ , i.e. so weak interdot tunneling that it provides the bottleneck for electron transport. As a consequence they typically describe the principal arcs correctly but all fail to predict additional higher order arcs, which are seen in experiments and found in complete numerical models [11, 13].

Within the approximation  $\Delta \ll \Gamma$ , we next generalize the approach introduced in Ref. [13] to include quasi-periodic driving. To describe the relevant interdot tunneling it is sufficient to consider one-electron states of the

DQD for which the second quantized Hamiltonian (1) in the localized basis reads

$$H(t) = \frac{\hbar}{2} \begin{pmatrix} \epsilon_0 + Af(t) & \Delta \\ \Delta & -\epsilon_0 - Af(t) \end{pmatrix}. \quad (14)$$

Assuming  $\Delta \ll \Gamma$  we treat the interdot tunneling  $\Delta$  within perturbation theory while considering the diagonal part,  $H_0(t) = \hbar[\epsilon_0 + Af(t)]\sigma_z/2$ , exactly. The corresponding interaction-picture Hamiltonian reads  $\tilde{H}(t) = U_0^\dagger(t)H_1U_0(t) = \hbar\tilde{\Delta}(t)\sigma_-/2 + \text{h.c.}$ , with  $H_1 = \Delta\sigma_x/2$ ,  $U_0(t)$  being the propagator corresponding to  $H_0(t)$ , and h.c. the Hermitian conjugate. The emerging time-dependent tunnel matrix element

$$\tilde{\Delta}(t) = e^{-i\epsilon_0 t - iAF(t)} \Delta \quad (15)$$

is governed by the dynamic phase  $\epsilon_0 t + AF(t)$  of the time evolution where  $dF/dt = f$ . For convenience, we choose the integration constant such that  $F(t)$  vanishes on average.

For the analytic analysis we assume that the tunnel processes are much slower than the driving (i.e. the non-adiabatic limit which does not influence the course of the principle arcs) and replace  $\tilde{\Delta}(t)$  by its time average  $\bar{\Delta}$ . Then according to Fermi's golden rule, we expect interdot tunneling with a rate  $\gamma \propto |\bar{\Delta}|^2/\Gamma$ , where the effective density of final states  $\propto 1/\Gamma$  reflects the broadening of the DQD states due to the dot-lead coupling  $\Gamma$ . Consequently, for  $\gamma \ll \Gamma$  the current through the DQD obeys the proportionality

$$I(\epsilon_0, A) \propto |\bar{\Delta}|^2 \propto \int dt dt' e^{i\epsilon_0(t-t') + iAF(t) - iAF(t')}, \quad (16)$$

where the integral may have to be regularized by an appropriate cutoff.

Notice that for a rigorous application of Fermi's golden rule, the final states must have a continuous spectrum. We achieve this by considering the relevant states of the still separate quantum dots after coupling them to the respective lead which yields a Lorentzian spectral density with a peak value  $2/\pi\Gamma$ . For an explicit calculation of a time-averaged current in this spirit, see Sec. 5.2 of Ref. [20]. Here we do not attempt to compute the prefactor, because it is irrelevant for the structure of the LZSM pattern.

To obtain the Fourier transformed pattern

$$\hat{I}(\tau_\epsilon, \tau_A) = \int d\epsilon_0 dA e^{-i\epsilon_0\tau_\epsilon - iA\tau_A} I(\epsilon_0, A) \quad (17)$$

we insert Eq. (16) and notice that both the  $\epsilon_0$ -integration and the  $A$ -integration yield delta functions. One of them reads  $\delta(\tau_\epsilon - t + t')$  and allows us to directly evaluate the  $t'$ -integral so that we remain with the expression

$$\hat{I}(\tau_\epsilon, \tau_A) \propto \int dt \delta(\tau_A - F(t + \tau_\epsilon/2) + F(t - \tau_\epsilon/2)) \quad (18)$$

$$\propto \sum_i \frac{1}{|f(t_i + \tau_\epsilon/2) + f(t_i - \tau_\epsilon/2)|}. \quad (19)$$

The sum has to be taken over all times  $t_i$  for which the argument of the delta function in Eq. (18) vanishes.

The two alternative expressions for  $\hat{I}(\tau_\epsilon, \tau_A)$  in Eqs. (18) and (19) provide the desired information about the interference pattern in Fourier space. First, Eq. (18) specifies the times  $t_i$  at which the delta function contributes. Second, Eq. (19) lets us conclude that the most significant contributions stem from regions in which the denominator vanishes. Thus, the structure in Fourier space is peaked on manifolds  $(\tau_\epsilon, \tau_A)$  on which the conditions

$$\tau_A = F(t + \tau_\epsilon/2) - F(t - \tau_\epsilon/2) \quad (20)$$

$$0 = f(t + \tau_\epsilon/2) - f(t - \tau_\epsilon/2) \quad (21)$$

are fulfilled. While these conditions are formally the same as those in Ref. [13], we like to emphasize that the present derivation extends their range of validity from periodic driving to quasi-periodic driving.

Henceforth we restrict ourselves to bichromatic driving of the form

$$f(t) = \sin(\Omega t) + \eta \sin(\Omega' t + \phi), \quad (22)$$

i.e., we augment the single-frequency driving by a further contribution with relative strength  $\eta$ , frequency  $\Omega'$ , and a phase shift  $\phi$ .

### 1. Commensurable frequencies

Commensurable frequencies generally result in periodic driving,  $f(t) = f(t + T)$ , where  $T$  is determined by the greatest common divisor of the frequencies. The corresponding solution of Eqs. (20) and (21) has been addressed in Ref. [13]. For later reference we outline its main aspects. First, the  $T$ -periodicity of  $f$  implies that if  $t_1$  solves Eq. (21), then  $t_2 = t_1 + T/2$  fulfills this condition as well. Therefore, the arcs come in pairs shifted by  $T/2$ , as is visible in Fig. 1(d). Second, generally Eq. (21) is transcendental and one has to resort to a numerical solution. Nevertheless, there exists a particular case that can be solved analytically. For a driving symmetric at  $t = t_0$ , i.e. for  $f(t_0 + t) = f(t_0 - t)$ , one finds the roots  $t_1 = t_0$  and  $t_2 = t_0 + T/2$ . They provide the arcs  $\tau_A^{(1)} = 2F(t_0 + \tau_\epsilon/2)$  and  $\tau_A^{(2)} = 2F(t_0 + T/2 + \tau_\epsilon/2)$ .

As in our experiment, we focus on the case

$$\Omega' = n\Omega \quad (23)$$

with integer  $n$ . Then  $f(t)$  is symmetric at  $t_0 = T/4$  for  $\phi = (\pm 1 - n)\pi/2$  and one finds the arcs

$$\tau_A^{(1,2)} = \pm \frac{2}{\Omega} \sin\left(\frac{\Omega\tau_\epsilon}{2}\right) + (-1)^n \frac{2\eta}{n\Omega} \sin\left(\frac{n\Omega\tau_\epsilon}{2}\right). \quad (24)$$

As we will see in both our numerical and in our measured data, the solution presented by Eq. (24) is incomplete even within the approximation  $\Delta \ll \Gamma$ . Depending on the value of the amplitude ratio  $\eta$  one may find further solutions [13].

### 2. Incommensurable frequencies

When  $\Omega$  and  $\Omega'$  are incommensurable, one cannot exploit symmetries such as periodicity and time-reversal. To nevertheless make progress, we insert the driving shape (22) into Eqs. (20) and (21) to obtain with the functional relations of the trigonometric functions the conditions

$$\tau_A = \frac{2}{\Omega} \sin(\Omega t) \sin\left(\frac{\Omega\tau_\epsilon}{2}\right) + \frac{2\eta}{\Omega'} \sin(\Omega' t + \phi) \sin\left(\frac{\Omega'\tau_\epsilon}{2}\right), \quad (25)$$

$$0 = \cos(\Omega t) \sin\left(\frac{\Omega\tau_\epsilon}{2}\right) + \eta \sin(\Omega' t + \phi) \cos\left(\frac{\Omega'\tau_\epsilon}{2}\right). \quad (26)$$

While it is practically impossible to determine all roots  $t_i$  of the second equation, we can restrict ourselves to those  $t_i$  for which both terms in Eq. (26) vanish individually. This happens when in each term the cosine becomes zero. Then the corresponding sines in Eq. (25) assume the values  $\pm 1$ . Therefore we can conjecture four arcs

$$\tau_A^{(\pm, \pm)} = \pm \frac{2}{\Omega} \sin\left(\frac{\Omega\tau_\epsilon}{2}\right) \pm \frac{2\eta}{\Omega'} \sin\left(\frac{\Omega'\tau_\epsilon}{2}\right), \quad (27)$$

where both  $\pm$  signs are independent of each other. Moreover, in accordance with the general deliberations below, the arcs turn out to be independent of  $\phi$ .

Thus, in contrast to the commensurable case, we find four independent arcs. While this reasoning does not exclude the existence of further solutions, our numerical and experimental results for  $\hat{I}(\tau_\epsilon, \tau_A)$  below confirm that the main structure of the Fourier transformed LZSM patterns for incommensurable frequencies is well described by Eq. (27).

### 3. Symmetries of the LZSM patterns

We start our symmetry considerations by noticing that the analytically predicted arcs for periodic driving in Eqs. (24) and quasi-periodic driving in Eq. (27) are all point symmetric with respect to the origin, i.e., they are invariant under the simultaneous inversion of the  $\tau_\epsilon$ -axis and the  $\tau_A$ -axis—a feature that extends beyond these two special cases. Indeed both the numerical and the measured Fourier transforms  $\hat{I}(\tau_\epsilon, \tau_A)$  of the interference patterns possess point symmetry, as can be appreciated in Figs. 3, 4, and 5.

Theoretically the point symmetry at the origin,  $\hat{I}(\tau_\epsilon, \tau_A) = \hat{I}(-\tau_\epsilon, -\tau_A)$ , is evident from the definition of  $\hat{I}(\tau_\epsilon, \tau_A)$  in Eq. (17) together with the analytic approximation (16) for the current: inverting in the definition the signs of  $\tau_\epsilon$  and  $\tau_A$  can be compensated by inverting in Eq. (16) the signs of  $\epsilon_0$  and  $A$  together with interchanging the integration variables  $t$  and  $t'$ . This is also seen in Eq. (18) which, owing to the symmetry of the delta function, is invariant under inverting the signs of both  $\tau_\epsilon$

and  $\tau_A$ . For the curves  $\tau_A(\tau_\epsilon)$  defined as the solutions of Eqs. (20) and (21), the point symmetry is manifest in the relation  $\tau_A(-\tau_\epsilon) = -\tau_A(\tau_\epsilon)$  which is obviously fulfilled by the explicit analytical predictions of the arcs in Eqs. (24) and (27).

For anti-symmetric driving with commensurable frequencies (e.g. for  $\Omega' = 2\Omega$  with  $\phi = 0$  or  $\pi$ ) we find in addition reflection symmetry at the  $\tau_A$ -axis, see Fig. 4. Together with the point symmetry discussed above, this implies reflection symmetry at the  $\tau_\epsilon$ -axis as well. In these specific cases, periodic bichromatic driving recovers the symmetry properties found for monochromatic driving. For a proof we notice that an anti-symmetric driving shape  $f(t) = -f(-t)$  corresponds to a symmetric  $F(t) = F(-t)$ . Then the integral in Eq. (18) is invariant under  $\tau_\epsilon \rightarrow -\tau_\epsilon$  since the sign of the integration variable  $t$  can be changed by substitution. With the same argument, we can invert in Eq. (16) the sign of the detuning  $\epsilon_0$ . Thus, in the validity regime of our analytical approximation, for anti-symmetric driving the interference pattern in real space,  $I(\epsilon_0, A)$ , must be symmetric with respect to the  $A$ -axis at  $\epsilon_0 = 0$ .

For driving with incommensurable frequencies we will see below that reflection symmetry in  $\tau_\epsilon$  and  $\tau_A$  is fully recovered. Our analytic conjecture (27) yields the striking result, that the arcs in Fourier space do not depend on the phase  $\phi$  between the driving components (we used this fact for testing the numerical implementation). This conjecture is confirmed by general considerations based on the fact that in ergodic systems time-averaged expectation values do not depend on a time offset. To demonstrate the independence of  $\phi$ , we consider a time delay by  $2\pi\ell/\Omega$  with integer  $\ell$ . This does not affect the first term in (27), while the second term acquires a phase  $\phi(\ell) = 2\pi\ell\Omega'/\Omega \pmod{2\pi}$ . For incommensurable  $\Omega$  and  $\Omega'$ , there always exists an integer  $n$  that brings  $\phi(\ell)$  arbitrarily close to a given  $2\pi - \phi$  for  $0 \leq \phi < 2\pi$ . This means that any phase  $\phi$  in  $f(t)$  can be compensated by a proper time shift, hence the time averaged expectation values are phase independent.

In the commensurable case, by contrast, the phase  $\phi(\ell) = 2\pi\ell\Omega'/\Omega \pmod{2\pi}$  assumes only a finite number of values given by the denominator  $k$  that appears when expressing the frequency ratio as a fraction of integers,  $\Omega'/\Omega = k'/k$  (for  $\Omega' = n\Omega$ , we have  $k = 1$  which implies  $\phi(\ell) = 0$  for all  $\ell$ ). Therefore, the phase in  $f(t)$  generally cannot be compensated by a time shift so that the interference patterns for periodic driving will depend on  $\phi$ .

This phase independence for incommensurable frequencies readily explains the reflection symmetry observed in Figs. 5(b),(d), which fully resembles the symmetry properties obtained for monochromatic driving. For  $\phi = \pi\Omega'/2\Omega$ , the driving shape  $f(t)$  is anti-symmetric. Therefore, according to the above reasoning for anti-symmetric driving (which did not make use of the commensurability), we can immediately conclude that the LZSM pattern must be reflection symmetric. Since the

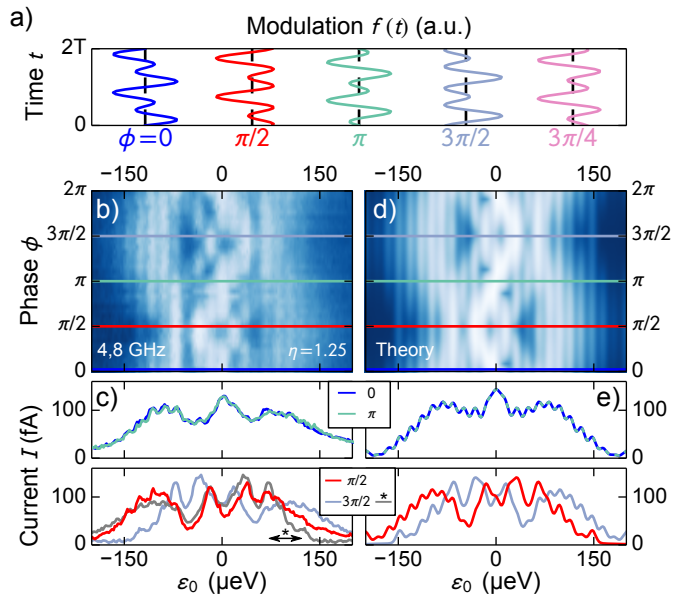


FIG. 2. (a) Shape of the ac driving,  $f(t) = \sin(\Omega t) + 1.25 \sin(2\Omega t + \phi)$ , for various phases  $\phi$ . For  $\phi = \pi/2$  and  $3\pi/2$ ,  $f(t)$  possesses reflection symmetry at specific times, for  $\phi = 0$  and  $\pi$ ,  $f(t)$  is anti-symmetric in time, while for other phases in the range  $0 \leq \phi < 2\pi$  symmetry is lost. (b) Phase dependent LZSM interference for  $f(t)$  as in (a), constant amplitude  $A = 57 \mu\text{eV}$ ,  $\eta = 1.25$  and  $\Omega/2\pi = 4 \text{ GHz}$  ( $\Omega' = 2\Omega$ ). (c) Interference patterns  $I(\epsilon_0)$  at the phases of enhanced symmetry along horizontal lines in (b) [color coded]. The gray line in the lower panel of (c) is the blueish curve after reflection at the  $\epsilon_0 = 0$ -axis. (d, e) Theory data corresponding to the measurements in (b, c) for interdot and dot-lead tunnel couplings  $\Delta = 8 \mu\text{eV}$  and  $\Gamma_L = \Gamma_R = 0.002 \mu\text{eV}$ , decoherence rate  $\gamma = 0.001 \mu\text{eV}$ , and inhomogeneous broadening  $\gamma^* = 5 \mu\text{eV}$ . Colorscales in panels (b) and (d) as in Fig. 1(c).

pattern does not depend on  $\phi$ , this symmetry for incommensurable frequencies must be generic.

Finally, let us emphasize that our symmetry considerations are based on the assumption that the two-level Hamiltonian (14) describes the relevant part of the transport process. In practice, the reflection symmetry with respect to the detuning may be compromised by dissipative processes or the influence of states not considered in our model. However, as we will see below, our measured results substantiate our simplifying approach by displaying a convincing agreement with our predictions.

## B. Results for commensurable frequencies

To test our general considerations above, we next consider a representative case of two commensurate frequencies, namely a fundamental mode and its second harmonic, i.e.,  $\Omega' = 2\Omega$ . In our experiment, the phase difference between the harmonics acquired along the dispersive transmission line through which we drive the gate voltages is not *a priori* known and has to be calibrated.



With this purpose we display in Fig. 2(b) the current as a function of the static detuning  $\epsilon_0$  and the phase  $\phi$  for the amplitude ratio  $\eta = 1.25$ .  $I(\epsilon_0, \phi)$  has maxima of constructive and minima of destructive interference. Closer inspection reveals varying symmetry properties of the interference pattern  $I(\epsilon_0)$  as function of  $\phi$  as expected from the symmetry considerations above.

To explore, how the symmetry of the interference is related to that of the driving function, in Fig. 2(a) we plot  $f(t)$  at five different phases. Generally,  $f(t)$  is asymmetric but it has enhanced symmetry at four special phases in the range  $0 \leq \phi < 2\pi$ :  $f(t)$  is reflection symmetric for  $\phi = \pi/2$  or  $3\pi/2$  and anti-symmetric for  $\phi = 0$  or  $\pi$  (with respect to distinct points along the time axis). For a direct comparison we present in Fig. 2(c) also  $I(\epsilon_0)$  at these four special phases, i.e. along the (color coded) horizontal lines in Fig. 2(b). The point symmetries of  $f(t)$  at  $\phi = 0$  or  $\pi$  expresses itself in  $I(\epsilon_0)$  as reflection symmetries, see upper panel of Fig. 2(c). In contrast to this anti-symmetric driving, reflection symmetry in  $f(t)$  at  $\phi = \pi/2$  or  $3\pi/2$  does not lead to a symmetric  $I(\epsilon_0)$ , see lower panel of Fig. 2(c). Moreover, the current traces are identical for  $\phi = 0$  and  $\pi$  but not for  $\phi = \pi/2$  and  $3\pi/2$ . However,  $I(\epsilon_0)$  at  $\phi = 3\pi/2$  matches that at  $\phi = \pi/2$  after reflection at  $\epsilon_0 = 0$  (gray curve). These differences are directly related to the symmetry properties of  $f(t)$  as we discussed in more detail in Sec. IV A 3 above. [Note that the measured  $I(\epsilon_0)$  curves are subject to a global asymmetry caused by higher order contributions to transport, such as co-tunneling via triplet states. This explains specifically the differences between the red curve (at  $\phi = \pi/2$ ) and the gray curve (at  $\phi = 3\pi/2$  and mirrored).]

Shifting the  $\phi$ -axis in panel (b) such that the symmetry properties match the corresponding phases concludes our phase calibration. Figures 2(d) and 2(e) display comparable theory data calculated as described in Sec. III B. The fit procedure allows us to determine important experimental parameters, namely the interdot and dot-lead couplings as well as decoherence and inhomogeneous broadening, see Ref. [11] for a discussion of a very similar fit procedure and the caption of Fig. 2 for fit parameters. The encountered parameters agree with our expectations from transport measurements and the agreement between the theory and experimental data is very good.

As an example of a LZSM interference pattern for bichromatic driving we present in Fig. 3 the current as a function of the driving amplitude  $A$  and the averaged detuning  $\epsilon_0$  for  $\Omega/2\pi = 4$  GHz,  $\Omega' = 2\Omega$ ,  $\eta = 2$ , and  $\phi = \pi/2$ . Measured data and their Fourier transform are presented in the upper panels and compared to numerical data below. In contrast to monochromatic driving (see Fig. 1) neither the data in real space (left) nor the Fourier transform (right) obey reflection symmetry but the Fourier transform has point symmetry, all in good agreement with theory [bottom panels] and with our expectations from Sec. IV A 3.

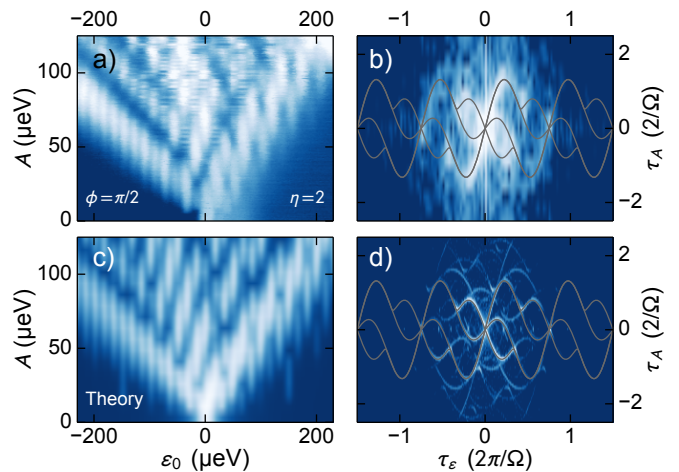


FIG. 3. Measured and computed LZSM pattern in real space (a,c) and in Fourier space (b,d) for the phase  $\phi = \pi/2$  and the amplitude ratio  $\eta = 2$ . All other parameters are as in Fig. 2, the colorscales are as in Fig. 1(c). The enhanced resolution of the theory data in Fourier space is achieved by considering data beyond the range shown in panel (c).

In real space [Figs. 3(a) and 3(c)], the patterns show clear resonance peaks which are located at detunings at which the energy quanta of the driving match the level splitting, i.e., when the condition  $(n\Omega)^2 = \Delta^2 + \epsilon_0^2$  is fulfilled for any integer  $n$ . The triangle in which the current assumes an appreciable value confirms the prediction given in Eq. (13), which follows from the condition that the amplitude must be so large that the time-dependent detuning  $\epsilon_0 + Af(t)$  reaches at least one avoided crossing. Since generally  $|\min f(t)| \neq |\max f(t)|$ , the parameter region in which interference takes place is asymmetric. In panels (a) and (c) of Fig. 3 we observe a clear tilt of the triangle to the left. This is a direct consequence of the asymmetry in driving with  $|\min f(t)| > |\max f(t)|$ , see Fig. 2(a). Within the triangle, the resonance lines are vertical and modulated. The physical pictures of the vanishing current at the minima is that of coherent destruction of tunneling [36, 37] which occurs when the time-average of the tunnel matrix element defined in Eq. (15) vanishes.

Figure 4 shows theoretical LZSM patterns in Fourier space for distinct phases chosen to emphasize the symmetry properties. As expected we always find point symmetry independent of the phase and, in addition, reflection symmetry for  $\phi = 0$  and  $\pi$  corresponding to antisymmetric driving  $f(-t) = -f(t)$ . Gradually increasing the phase from 0 to  $\pi$  (or from  $\pi$  to  $2\pi$ ) first distorts the patterns and then brings them back to their original shape.

Concerning the semi-analytical calculation of the arcs structure (gray lines), these results confirm the predictions of Ref. [13]. There however, the patterns depict the non-equilibrium population of a driven spin-boson model, while the present results stem from a transport theory for an open DQD which allows for particle exchange between



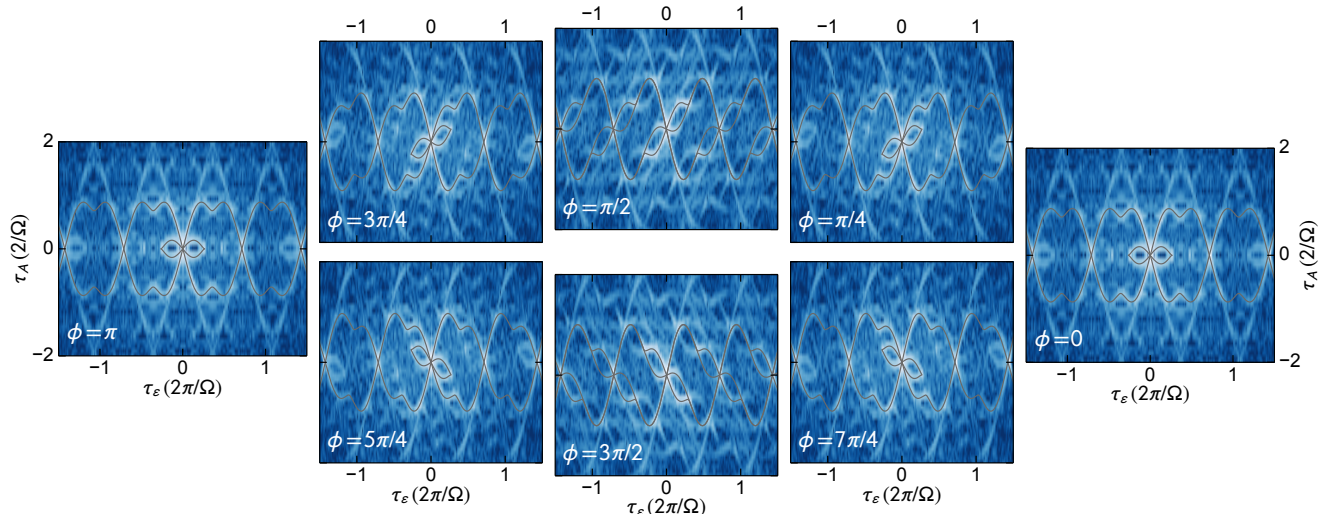


FIG. 4. Theoretical LZSM patterns in Fourier representation for bichromatic driving with commensurable frequencies for various relative phases. The driving frequencies are  $\Omega/2\pi = 4$  GHz and  $\Omega'/2\pi = 8$  GHz, while the amplitude ratio is  $\eta = 1.25$ . The gray lines are the solutions of Eqs. (20) and (21). The phases  $\phi = \pi/2$  and  $\phi = 3\pi/2$  correspond to symmetric driving for which part of the structure is given by the analytic expression (24).

the system and fermionic reservoirs. Therefore, we can conclude that a simple description with a closed two-level model provides a valid prediction of LZSM patterns also for open systems.

### C. Results for incommensurable frequencies

Finally, we present our results for the case of incommensurate frequencies. Because of the finite broadening one might ask the question of how well we can experimentally (and numerically) differentiate between the periodic and the quasi-periodic case. For practical purposes, the numerical calculations are performed with rational approximations with a finite number of digits. We nevertheless use the terms “irrational” and “incommensurable”. The differences to the commensurable case is typically best visible if one chooses for  $\Omega'/\Omega$  the “most irrational number”, namely the golden ratio  $g = (1+\sqrt{5})/2 \simeq 1.618$  [38].

In Fig. 5 we present measured and calculated data for  $\Omega'/\Omega = g$ . As expected from our discussion in Sec. IV A 3 for incommensurable frequencies the data in real space recover reflection symmetry in respect to the  $A$ -axis at  $\epsilon_0 = 0$  while the Fourier transform exhibits reflection symmetry in regard to both axis. A further remarkable difference to the commensurable case with vertical resonance lines of enhanced current in the real space interference pattern is that the latter are tilted while the pattern nevertheless shows a regular structure. The agreement between theory and experiment is good even on a quantitative level.

In Fourier space [see Figs. 5(b),(d)], the arcs follow by and large the prediction in Eq. (27) (gray lines). Taking

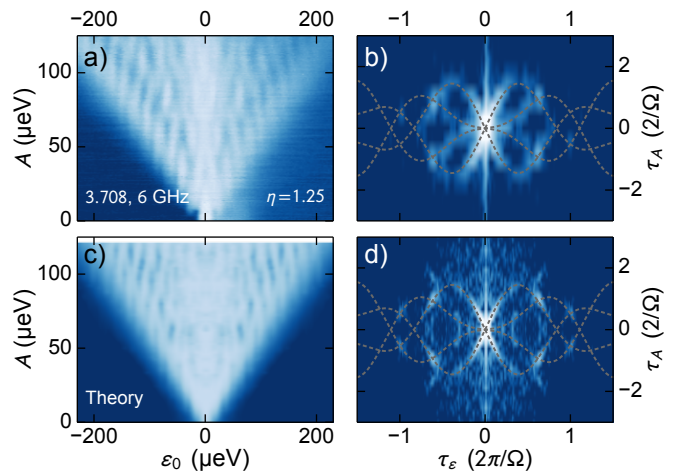


FIG. 5. Experiment (a, b) and theory (c, d) for the driving frequencies  $\Omega = 3.708$  GHz,  $\Omega' = 6$  GHz and the amplitude ratio  $\eta = 1.25$ . The frequency ratio approximates the golden mean with a precision of  $10^{-4}$ . All other parameters are as in Fig. 2, the colorscales are as in Figs. 1(c, d). Dashed lines visualize the analytical prediction in Eq. (27).

into account that the analytical derivation of the structure was based on the *ad hoc* assumption that the main contribution stems from those roots of Eq. (26) for which both terms vanish individually, the agreement between measured and calculated data in Fourier space is surprisingly good. Note that the stronger broadening of the measured data in Fourier space compared to the calculated ones is mainly caused by the smaller range probed for  $\epsilon_0$  and  $A$  in real space, which determines the resolution in Fourier space.

## V. CONCLUSIONS

We have extended theoretically and experimentally LZSM interference from the already known monochromatic case to bichromatic driving. Studying quantum transport through a strongly biased DQD ( $V = 1$  mV), we measured the dc current in the steady state and explored LZSM interference as a function of the DQD detuning and the driving amplitude.

The interference patterns in our measurements and their two-dimensional Fourier transforms exhibit characteristic symmetry properties which we have confirmed in our analytical and numerical predictions: bichromatic driving with commensurable frequencies causes a reduction of the symmetry compared to the monochromatic case (except for two specific phase relations, only point symmetry in Fourier space survives). Interestingly, for driving with incommensurable frequencies the full reflection symmetries observed for monochromatic driving are retained, although the interference patterns are more complex.

Our theoretical approaches exploit the Floquet theorem for time-dependent master equations that include the incoherent dot-lead tunneling. For the periodic driving with commensurable frequencies, the long-time solution obeys the periodicity of the Liouvillian and, thus, can be decomposed into a Fourier series. Then the master equation can be written with the help of a blockdiagonal Floquet matrix. For the quasiperiodic driving with two incommensurable frequencies, we have developed an efficient numerical scheme for the computation of the long-time solution. It is based on a two-color Floquet theory for which we have combined a Floquet matrix decomposition with ideas adopted from the  $t$ - $t'$  formalism. In doing so, we have mapped the bichromatically time-dependent master equation to a monochromatically driven problem in a higher dimensional space. This allowed us to find a solution based on known Floquet methods for periodic driving.

Experimentally, the phase dependence of the interference patterns for bichromatic driving with commensurable frequencies can be used to accurately calibrate phase differences caused by frequency dispersion. This is an important advantage for quantum measurements and related applications in quantum information where accurate knowledge of phase relations is crucial. To properly fit our measured interference patterns in our model we needed to take into account decoherence and an inhomogeneous line broadening. Our results here quantitatively confirm our earlier findings in a similar system [11].

We have theoretically predicted and experimentally confirmed a strong relevance of commensurability effects in coherent nanoelectronics. Our results will be relevant for applications based on coherent driving with more than one frequency.

## ACKNOWLEDGMENTS

We thank Mónica Benito for helpful discussions. This work was supported by the Spanish Ministry of Economy and Competitiveness through Grant No. MAT2014-58241-P and by the DFG via LU 819/4-1, SFB 631, and the Cluster of Excellence “Nanosystems Initiative Munich (NIM)”. SL acknowledges support via a Heisenberg fellowship.

### Appendix A: Additional data

#### 1. Commensurate frequencies for various phases

In Fig. 6 we present additional measured data for three different phases at  $\Omega' = 2\Omega$ . The data clearly confirm the predicted point symmetries, albeit the Fourier transformation causes an additional broadening due to with a relatively small amount of data points. The theoretical predictions for the arcs result from a numerical solution of Eqs. (20) and (21). They are in accordance with the structure observed in the measured data.

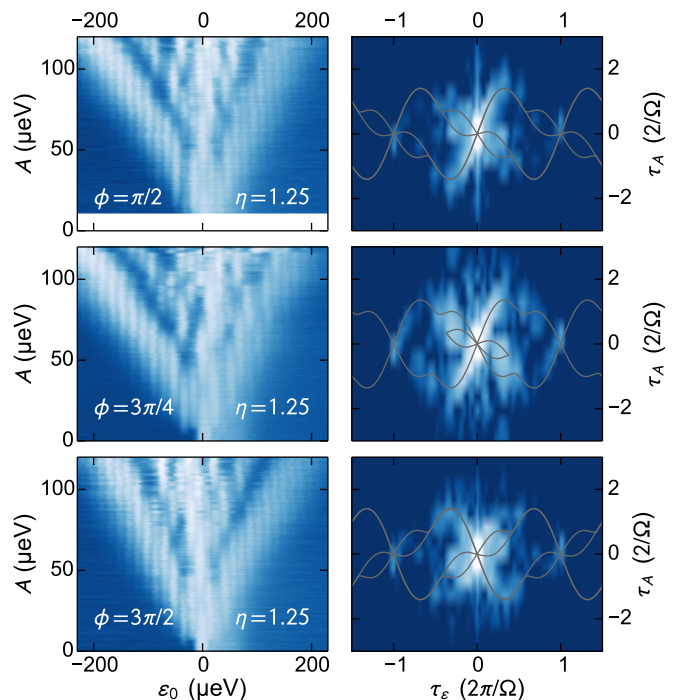


FIG. 6. Measured LZSM pattern in real space and in Fourier space for commensurable frequencies  $\Omega/2\pi = 4$  GHz and  $\Omega'/2\pi = 8$  GHz and the phases and amplitude ratios displayed in the graphics. The gray lines indicate the arcs predicted by Eqs. (20) and (21).

## 2. Further combinations of incommensurate frequencies

Figure 7 depicts further experimental data for incommensurate frequencies. In the upper row, the frequency ratio is the golden mean,  $\Omega'/\Omega = g$ . As compared to Fig. 5, the frequencies are slightly smaller, while the amplitude ratio  $\eta$  is significantly larger. In the lower row, the frequency ratio is twice the golden mean,  $\Omega'/\Omega = 2g$ . The findings are consistent with the predictions in Sec. IV C: they confirm the symmetry in real space (left column), and the theoretical prediction (27) for the arcs in Fourier space (right column). Moreover, the Fourier transform of the pattern is most pronounced when two arcs cross each other.

### Appendix B: Floquet theory for master equations with monochromatic driving

We consider the periodically time-dependent master equation  $\dot{P} = L(t)P$  with a Liouvillian of the form

$$L(t) = L_0 + L_1 \cos(\Omega t + \varphi). \quad (\text{B1})$$

In the case of a quantum master equation, the “distribution function” is the reduced density operator, which generally possesses off-diagonal matrix elements. We are interested in its long-time limit, the steady-state solution  $P_\infty(t)$ . Due to the linearity of the master equation, the steady state solution obeys the periodicity of the Liouvillian, i.e.,

$$P_\infty(t) = P_\infty(t + 2\pi/\Omega) = \sum_k p_k e^{-ik\Omega t}. \quad (\text{B2})$$

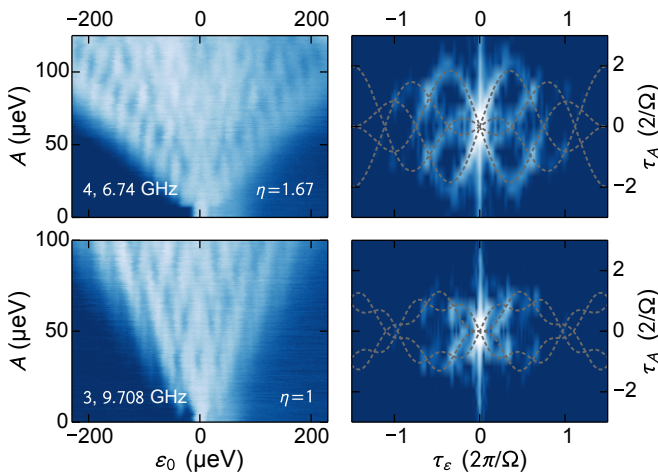


FIG. 7. Measured LZSM pattern in real space and in Fourier space for the incommensurate frequencies with ratios  $g$  (the golden mean) and  $2g$  and amplitude ratios displayed in the graphics. The gray lines indicate the arcs predicted by Eq. (27).

The trace condition of the density operator leads for the Fourier coefficients to the normalization  $\text{tr} p_k = \delta_{k,0}$ . Our main interest lies in time-averaged expectation values where the time-dependence is fully contained in the density operator  $P_\infty(t)$ . Hence,  $\overline{P_\infty(t)} = p_0$  contains all relevant information.

### 1. Master equation in Sambe space

A conceptually straightforward way to compute the  $p_k$  is to write the master equation in Fourier space where it reads  $\sum_{k'} \mathcal{L}_{kk'} p_{k'} = 0$ , where  $\mathcal{L}$  denotes the Fourier representation of the superoperator  $\mathcal{L} = L(t) - \partial/\partial t$  with the components [24]

$$\mathcal{L}_{kk'} = (L_0 + ik\Omega)\delta_{kk'} + \frac{L_1}{2}(e^{i\varphi}\delta_{k+1,k'} + e^{-i\varphi}\delta_{k-1,k'}). \quad (\text{B3})$$

It can be written as tridiagonal block matrix, the so-called Floquet matrix. Its diagonal blocks are  $L_0 + ik\Omega$ , while its first diagonals is given by the driving  $L_1$ . The kernel of the Floquet matrix is a vector that contains the Fourier coefficients  $p_k$  of the steady state solution. The Fourier representation of the Liouvillian can be understood as extending the space in which the density operator is defined by the space of  $2\pi/\Omega$ -periodic functions (Sambe space) [23, 39]. For numerical computations, one has to truncate the Floquet matrix setting  $p_k = 0$  for all  $k < -k_0$  and  $k > k_0$ . For a driving amplitude  $A$ , the value at which one reaches numerical convergence usually scales as  $k_0 \propto A/\Omega$ .

In the presence of higher harmonics  $L(t) \rightarrow L(t) + L_n \cos(n\Omega t + \varphi_n)$  with a phase lag  $\varphi_n$ , the  $n$ th secondary diagonals become

$$\frac{L_n}{2}(e^{i\varphi_n}\delta_{k+n,k'} + e^{-i\varphi_n}\delta_{k-n,k'}). \quad (\text{B4})$$

For a generalization of this method to the case of two commensurable driving frequencies  $\Omega_i$ , one works in the Sambe space whose frequency  $\Omega$  is a common divisor of the  $\Omega_i$  such that  $\Omega_i = n_i\Omega$ . Then the secondary diagonals with indices  $n_i$  are non-vanishing.

### 2. Matrix-continued fraction

For large driving amplitudes or small frequencies, the Floquet matrix can become quite large. Then a more efficient way to compute the steady state  $p_0$  is the matrix-continued fraction method widely applied in the context of Brownian motion [40, 41]. For the single-frequency driving underlying the Floquet matrix (B3), it is based on the fact that the linear equation for the Fourier coefficients  $p_k$  corresponds to the tridiagonal recurrence relation

$$e^{i\varphi} B p_{k+1} + A_k p_k + e^{-i\varphi} B p_{k-1} = 0 \quad (\text{B5})$$

where  $A_k = L_0 + ik\Omega$  and  $B = L_1/2$ . The truncation of the Floquet matrix (B3) corresponds to assuming  $p_k = 0$  for  $|k| > k_0$ .

The direct solution of the recurrence relation (B5) is hindered by the fact that the matrix  $B$  generally does not possess an inverse. This problem can be circumvented by defining transfer matrices  $S_k$  and  $R_k$  via

$$p_k = \begin{cases} R_k e^{i\varphi} B p_{k+1} & \text{for } k < 0, \\ S_k e^{-i\varphi} B p_{k-1} & \text{for } k > 0. \end{cases} \quad (\text{B6})$$

This allows us to substitute in the recurrence relation the terms  $B p_{k\pm 1}$  by expressions proportional to  $p_k$ . Compli-

ance of this ansatz with Eq. (B5) is ensured for

$$S_k = -(A_k + B S_{k+1} B)^{-1}, \quad (\text{B7})$$

$$R_k = -(A_k + B R_{k-1} B)^{-1}, \quad (\text{B8})$$

while  $p_0$  obeys

$$(B R_{-1} B + A_0 + B S_1 B) p_0 = 0. \quad (\text{B9})$$

In a numerical calculation, one starts with  $S_{k_0+1} = R_{-(k_0+1)} = 0$  and iterates Eqs. (B7) and (B8) to obtain  $S_1$  and  $R_{-1}$ . Finally one obtains  $p_0$  by solving Eq. (B9) under the trace condition  $\text{tr } p_0 = 1$ . Notice that the iteration scheme and, thus, the time averaged steady-state distribution do not depend on  $\varphi$ .

- 
- [1] W. D. Oliver, Y. Yu, J. C. Lee, K. K. Berggren, L. S. Levitov, and T. P. Orlando, *Science* **310**, 1653 (2005).
- [2] M. Sillanpää, T. Lehtinen, A. Paila, Y. Makhlin, and P. Hakonen, *Phys. Rev. Lett.* **96**, 187002 (2006).
- [3] C. M. Wilson, T. Duty, F. Persson, M. Sandberg, G. Johansson, and P. Delsing, *Phys. Rev. Lett.* **98**, 257003 (2007).
- [4] M. S. Rudner, A. V. Shytov, L. S. Levitov, D. M. Berns, W. D. Oliver, S. O. Valenzuela, and T. P. Orlando, *Phys. Rev. Lett.* **101**, 190502 (2008).
- [5] D. M. Berns, M. S. Rudner, S. O. Valenzuela, K. K. Berggren, W. D. Oliver, L. S. Levitov, and T. P. Orlando, *Nature (London)* **455**, 51 (2008).
- [6] A. Izmalkov, S. H. W. van der Ploeg, S. N. Shevchenko, M. Grajcar, E. Il'ichev, U. Hübner, A. N. Omelyanchouk, and H.-G. Meyer, *Phys. Rev. Lett.* **101**, 017003 (2008).
- [7] J. Li, M. P. Silveri, K. S. Kumar, J.-M. Pirkkalainen, A. Vepsäläinen, W. C. Chien, J. Tuorila, M. A. Sillanpää, P. J. Hakonen, E. V. Thuneberg, and G. S. Paraoanu, *Nature Comm.* **4**, 1420 (2013).
- [8] M. P. Silveri, K. S. Kumar, J. Tuorila, J. Li, A. Vepsäläinen, E. V. Thuneberg, and G. S. Paraoanu, *New J. Phys.* **17**, 043058 (2015).
- [9] J. Stehlik, Y. Dovzhenko, J. R. Petta, J. R. Johansson, F. Nori, H. Lu, and A. C. Gossard, *Phys. Rev. B* **86**, 121303(R) (2012).
- [10] E. Dupont-Ferrier, B. Roche, B. Voisin, X. Jehl, R. Wacquez, M. Vinet, M. Sanquer, and S. De Franceschi, *Phys. Rev. Lett.* **110**, 136802 (2013).
- [11] F. Forster, G. Petersen, S. Manus, P. Hänggi, D. Schuh, W. Wegscheider, S. Kohler, and S. Ludwig, *Phys. Rev. Lett.* **112**, 116803 (2014).
- [12] S. Platonov, B. Kästner, H. W. Schumacher, S. Kohler, and S. Ludwig, *Phys. Rev. Lett.* **115**, 106801 (2015).
- [13] R. Blattmann, P. Hänggi, and S. Kohler, *Phys. Rev. A* **91**, 042109 (2015).
- [14] K. M. Fonseca-Romero, S. Kohler, and P. Hänggi, *Chem. Phys.* **296**, 307 (2004).
- [15] T. M. Stace, A. C. Doherty, and S. D. Barrett, *Phys. Rev. Lett.* **95**, 106801 (2005).
- [16] S. N. Shevchenko, S. Ashhab, and F. Nori, *Phys. Rep.* **492**, 1 (2010).
- [17] Y. Kayanuma, *Phys. Rev. A* **50**, 843 (1994).
- [18] A. Ferrón, D. Domínguez, and M. J. Sánchez, *Phys. Rev. Lett.* **109**, 237005 (2012).
- [19] M. Strass, P. Hänggi, and S. Kohler, *Phys. Rev. Lett.* **95**, 130601 (2005).
- [20] S. Kohler, J. Lehmann, and P. Hänggi, *Phys. Rep.* **406**, 379 (2005).
- [21] P. Hänggi, in *Quantum Transport and Dissipation* (Wiley-VCH, Weinheim, 1998) Chap. 5, pp. 249–286.
- [22] S. I. Chu and D. A. Telnov, *Phys. Rep.* **390**, 1 (2004).
- [23] H. Sambe, *Phys. Rev. A* **7**, 2203 (1973).
- [24] T.-S. Ho, K. Wang, and S.-I. Chu, *Phys. Rev. A* **33**, 1798 (1986).
- [25] K. Ono, D. G. Austing, Y. Tokura, and S. Tarucha, *Science* **297**, 1313 (2002).
- [26] F. Forster, M. Mühlbacher, D. Schuh, W. Wegscheider, and S. Ludwig, *Phys. Rev. B* **91**, 195417 (2015).
- [27] H.-P. Breuer and F. Petruccione, *Theory of open quantum systems* (Oxford University Press, Oxford, 2003).
- [28] T. Brandes, *Phys. Rep.* **408**, 315 (2005).
- [29] U. Weiss and M. Wollensak, *Phys. Rev. Lett.* **62**, 1663 (1989).
- [30] U. Peskin and N. Moiseyev, *J. Chem. Phys.* **99**, 4590 (1993).
- [31] L. D. Landau, *Phys. Z. Sowjetunion* **2**, 46 (1932).
- [32] C. Zener, *Proc. R. Soc. London, Ser. A* **137**, 696 (1932).
- [33] E. C. G. Stueckelberg, *Helv. Phys. Acta* **5**, 369 (1932).
- [34] E. Majorana, *Nuovo Cimento* **9**, 43 (1932).
- [35] L. Arrachea and M. Moskalets, *Phys. Rev. B* **74**, 245322 (2006).
- [36] F. Grossmann, T. Dittrich, P. Jung, and P. Hänggi, *Phys. Rev. Lett.* **67**, 516 (1991).
- [37] F. Großmann and P. Hänggi, *Europhys. Lett.* **18**, 571 (1992).
- [38] H. G. Schuster, *Deterministic Chaos: An Introduction* (VCH Verlagsgesellschaft, Weinheim, 1995).
- [39] J. H. Shirley, *Phys. Rev.* **138**, B979 (1965).
- [40] H. Risken, *The Fokker-Planck equation*, 2nd ed., Springer Series in Synergetics, Vol. 18 (Springer, Berlin, 1989).
- [41] P. Jung, *Phys. Rep.* **234**, 175 (1993).